

## RESEARCH ARTICLE

10.1002/2014JA019763

## Key Points:

- An Alfvénic boundary condition for magnetosphere-ionosphere coupling is given
- Coupling is self-consistent and nonlinear, and ionosphere is resolved in altitude
- Numerical solutions are presented to demonstrate the boundary condition

## Correspondence to:

A. N. Wright,  
anw@st-and.ac.uk

## Citation:

Wright, A. N., and A. J. B. Russell (2014), Alfvén wave boundary condition for responsive magnetosphere-ionosphere coupling, *J. Geophys. Res. Space Physics*, 119, doi:10.1002/2014JA019763.

Received 9 JAN 2014

Accepted 19 APR 2014

Accepted article online 24 APR 2014

## Alfvén wave boundary condition for responsive magnetosphere-ionosphere coupling

Andrew N. Wright<sup>1</sup> and Alexander J. B. Russell<sup>2</sup>
<sup>1</sup>Mathematical Institute, University of St. Andrews, St. Andrews, UK, <sup>2</sup>Division of Mathematics, University of Dundee, Dundee, UK

**Abstract** The solution of electric fields and currents in a height-resolved ionosphere is traditionally solved as an elliptic equation with Dirichlet or Neumann boundary condition in which the magnetosphere is represented as an unresponsive (prescribed) voltage generator or current source. In this paper we derive an alternative boundary condition based upon Alfvén waves in which only the Alfvén wave from the magnetosphere that is incident upon the ionosphere ( $E_{xi}$ ) is prescribed. For a uniform magnetosphere the new boundary condition reduces to

$$\partial\phi/\partial z = (\partial^2\phi/\partial x^2 + 2\partial E_{xi}/\partial x)/(\mu_0 V_A \sigma_{\parallel})$$

and is evaluated at the magnetosphere-ionosphere interface. The resulting solution is interpreted as a responsive magnetosphere and establishes a key stage in the full self-consistent and nonlinear coupling of the magnetosphere and ionosphere.

## 1. Introduction

From the perspective of the magnetosphere, the ionosphere represents a lower boundary. In its simplest form this can be taken as a highly conducting reflective sheet, although a more sophisticated treatment allows for the description of a partially reflected Alfvén wave through the use of height-integrated conductivities.

The closure of magnetospheric field-aligned currents in the ionosphere can redistribute ionospheric plasma and significantly modify the associated conductivity and resultant coupling. This process has been studied from a number of different viewpoints: *Doe et al.* [1995] and *Zettergren and Semeter* [2012] consider a resolved (not sheet) ionosphere and assumed the voltage at the magnetosphere-ionosphere interface as being known. A complementary study by *Karlsson and Marklund* [1998] prescribed the normal current at the interface. While these models allow changing ionospheric conductivity, they maintained given boundary conditions and so did not represent a “responsive” magnetosphere. The latter aspect has been addressed by *Lysak and Song* [2002], *Cran-McGreehin et al.* [2007], and *Russell et al.* [2010] by representing the magnetospheric solution as incident Alfvén wave plus a reflected wave from the ionosphere. When the ionospheric conductivity is modified through current closure, the reflected wave, and hence magnetospheric solution, are modified in a self-consistent fashion. This whole process is nonlinear and can lead to steepening and the formation of discontinuities, unless electron inertial effects are retained. [*Russell and Wright*, 2012; *Russell et al.*, 2013].

The self-consistent responsive magnetosphere models described above permit considerable progress but adopt the simplification of a sheet ionosphere and work with height-integrated conductivities. In contrast, the “unresponsive” magnetosphere models resolve spatial structure within the ionosphere. The purpose of the current paper is to establish a boundary condition for a resolved ionosphere that can represent a responsive magnetosphere, and so retain the best aspects of both modeling approaches.

## 2. Model

The model we adopt is two-dimensional, like the previous studies, and is shown schematically in Figure 1. The whole system is independent of  $y$  ( $\partial/\partial y = 0$ ) and has a vertical static background magnetic field  $\mathbf{B}_0 = (0, 0, -B_0)$ . The solution depends upon the horizontal coordinate  $x$  and the vertical coordinate  $z$ . We choose  $z = 0$  to coincide with the base of the ionospheric section which has a vertical extent  $h$ . The

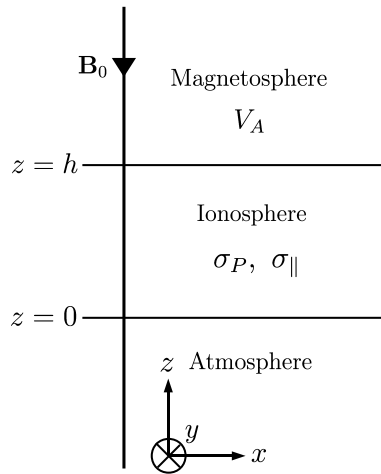


**Figure 1.** Schematic of the model. An ideal magnetosphere characterized by an Alfvén speed  $V_A$  is situated above a distributed ionosphere ( $0 < z < h$ ). The system is driven by an incident Alfvén wave with fields  $E_{xi}(x)\hat{x}$  and  $b_{yi}(x)\hat{y}$ . The solution is invariant in the  $y$  direction.

and assume  $E_{xi}$  to be a suitable prescribed function. However,  $E_{xr}$  (and  $b_{yr}$ ) are determined by reflection from a structured ionosphere. Hence, the total solution in the magnetosphere

$$E_x = E_{xi} + E_{xr} \quad \text{and} \quad b_y = b_{yi} + b_{yr} \quad (4)$$

responds to the ionosphere and any changes in conductivity in a self-consistent fashion.

The solution throughout the ionosphere is described through the use of Pedersen and parallel conductivities ( $\sigma_P$  and  $\sigma_{\parallel}$ ),

$$\mathbf{j} = \boldsymbol{\sigma} \cdot \mathbf{E} \implies j_x = \sigma_P E_x, \quad j_z = \sigma_{\parallel} E_z. \quad (5)$$

For the low-frequency solutions that we consider, an electrostatic potential may be adopted in the ionosphere,

$$\mathbf{E} = -\nabla\phi. \quad (6)$$

### 2.1. Height-Integrated Conductivities

To benchmark our model, we expect to be able to recover the height-integrated conductivity model in an appropriate limit. The familiar analytical results are easily obtained by integrating (5) over  $0 < z < h^+$  and using Ampère's Law to give

$$\mu_0 \int_0^{h^+} j_x dz = \mu_0 \int_0^{h^+} E_x(x, z) \sigma_P(x, z) dz = -b_y(x, z = h^+) \quad (7)$$

where  $b_y(x, z = h^+)$  is the magnetic field at the base of the magnetosphere when we assume  $b_y(x, z = 0) = 0$ . Combined with equation (3), this may be written as

$$-(b_{yi} + b_{yr}) = \mu_0 E_x(x, h^+) \Sigma_P, \quad (8)$$

where

$$\Sigma_P(x) = \int_0^h \frac{E_x(x, z)}{E_x(x, h^+)} \sigma_P(x, z) dz. \quad (9)$$

magnetosphere-ionosphere interface is located at  $z = h$ , and we will make a distinction between quantities evaluated at the base of the magnetosphere ( $z = h^+$ ) and at the top of the ionosphere ( $z = h^-$ ).

The magnetosphere is described by the single-fluid ideal MHD approximation (which assumes that the transverse scales are larger than the electron inertial length and the ion gyroradius) and has incident and reflected Alfvén wave fields at  $z = h^+$  denoted by

$$\text{Incident wave: } E_{xi}\hat{x}, b_{yi}\hat{y} \quad (1)$$

$$\text{Reflected wave: } E_{xr}\hat{x}, b_{yr}\hat{y} \quad (2)$$

which have the properties given by Walén [1944]

$$E_{xi} = -b_{yi}V_A, \quad E_{xr} = +b_{yr}V_A. \quad (3)$$

Here  $V_A$  is the Alfvén speed at  $z = h^+$ . Note that the fields and  $V_A$ , although evaluated at  $z = h^+$ , may be functions of  $x$  and  $t$  in general. Typically, we expect  $E_{xi}$  (and hence  $b_{yi}$ ) to be determined by processes in the magnetosphere

Here  $\Sigma_p$  is the height-integrated Pedersen conductivity weighted by  $E_x$  relative to its value at  $z = h^+$ . In the limit of sufficiently high  $\sigma_{\parallel}$ , there is negligible potential drop along  $\mathbf{B}$ , so magnetic field lines are equipotentials and  $E_x(x, z) \approx E_x(x, h^+)$ , i.e., is independent of  $z$ . In this case the weighting factor is unity, and we recover the much used result

$$\Sigma_p(x) \approx \int_0^h \sigma_p(x, z) dz. \quad (10)$$

Recalling that  $E_x(x, h^+) = E_{xi} + E_{xr}$ , and using the relations in (3), equation (8) becomes

$$E_{xi} - E_{xr} = \mu_0 V_A \Sigma_p (E_{xi} + E_{xr}). \quad (11)$$

Hence, the reflection properties may be characterized with

$$\frac{E_{xr}}{E_{xi}} = \frac{1 - \Sigma_p / \Sigma_A}{1 + \Sigma_p / \Sigma_A} \quad (12)$$

or

$$\frac{E_x(x, h^+)}{E_{xi}} = \frac{2}{1 + \Sigma_p / \Sigma_A}, \quad (13)$$

where  $\Sigma_A = 1/(\mu_0 V_A)$  is the Alfvén conductance.

## 2.2. Conductivity Values

Kelley [2009] shows how typical  $E$  region Pedersen conductivities range from  $5 \times 10^{-6}$  (night) to  $5 \times 10^{-4}$  (day) mho/m. For an  $E$  region thickness of 20 km, these suggest that the range of height-integrated Pedersen conductivities is  $0.1 < \Sigma_p < 10$  mho. The parallel conductivity decreases rapidly over the  $E$  region, and Kelley [2009] gives a daytime value (at 120 km altitude) of around 2 mho/m, which may be scaled to give a nighttime value of  $2 \times 10^{-2}$  mho/m owing to lower electron densities.

We shall also need the Alfvén speed at the base of the magnetosphere, which may be taken as the bottom of the  $F$  region for illustrative purposes. Here the electron density varies between  $10^{11} \text{ m}^{-3}$  (daytime) and  $10^9 \text{ m}^{-3}$  (nighttime) according to Rees [1989]. To estimate representative Alfvén speeds ( $V_A$ ), we assume quasi-neutrality and take a mean ion mass of around 20 amu, suggesting that  $V_A$  is in the range  $3 \times 10^5$  (day) to  $3 \times 10^6$  (night)  $\text{ms}^{-1}$ . The corresponding Alfvén conductivities are 2.7 (day) and 0.27 (night) mho. Hence, the ratio of conductances is

$$0.4 < \Sigma_p / \Sigma_A < 4, \quad (14)$$

indicating that the ionosphere can act as a highly conducting reflecting boundary on the dayside, but more like an insulating boundary on the nightside. Of course, there are more sophisticated routes to estimating the Alfvén and Pedersen conductivities which may extend the limits given in (14) to 0.1 at night and 10 during the daytime. However, the conclusion that the ionosphere has the capacity to act as a highly insulating or highly conducting boundary remains unchanged. This paper develops and tests the implementation of a distributed ionosphere model coupled to a magnetosphere that can accommodate these parameter ranges.

## 3. Coupled Model and Interface Condition

The structured ionosphere may be described in terms of conductivities  $\sigma_p(x, z)$  and  $\sigma_{\parallel}(x, z)$ , as indicated in equations (5) and (6), which allows an elliptic potential formulation given quasi-neutrality ( $\nabla \cdot \mathbf{j} = 0$ )

$$\frac{\partial}{\partial x} \left( \sigma_p \frac{\partial \phi}{\partial x} \right) + \frac{\partial}{\partial z} \left( \sigma_{\parallel} \frac{\partial \phi}{\partial z} \right) = 0. \quad (15)$$

As mentioned previously, this equation is normally solved by defining  $\phi$  (or its normal derivative) on the boundary of the ionosphere. Such a condition represents an unresponsive magnetosphere which supplies a given voltage (or current) regardless of how the ionosphere evolves. Here we show how the Alfvén fields in equations (1)–(3) can represent a responsive magnetosphere in which only the Alfvén wave from the magnetosphere that is incident upon the ionosphere is prescribed.

The Alfvén wave reflection coefficient  $r(x)$  is defined in terms of the fields at  $z = h^+$

$$r(x) = \frac{E_{xr}(x, h^+)}{E_{xi}(x, h^+)}. \quad (16)$$

Employing (3) and (16), the total Alfvén fields at  $z = h^+$  may be defined as follows:

$$\begin{aligned} E_x^+ &= E_{xi} + E_{xr} = E_{xi}(1 + r), \\ b_y^+ &= b_{yi} + b_{yr} = b_{yi}(1 - r). \end{aligned} \quad (17)$$

Eliminating  $r$  between the  $E_x^+$  and  $b_y^+$  equations above and eliminating  $b_{yi}$  using (3) gives

$$b_y^+ = (E_x^+ - 2E_{xi}) / V_A. \quad (18)$$

We are now in a position to evaluate  $j_z^+ = j_z(x, h^+)$  by taking the curl of  $b_y^+ \hat{y}$  using (18) and also  $j_z^- = j_z(x, h^-)$  from (5) and (6). Since  $j_z$  is continuous across  $z = h$ , we conclude

$$j_z^+ = \frac{1}{\mu_0} \frac{\partial b_y^+}{\partial x} = \frac{1}{\mu_0} \frac{\partial}{\partial x} \left( \frac{E_x^+ - 2E_{xi}}{V_A} \right) = -\sigma_{\parallel} \frac{\partial \phi}{\partial z} = j_z^-. \quad (19)$$

The tangential electric field is also continuous across  $z = h$ . Hence,

$$E_x^+ \equiv -\frac{\partial \phi}{\partial x} \Big|_{z=h^-}, \quad (20)$$

and eliminating  $E_x^+$  between (19) and (20) gives our final interface condition

$$\frac{\partial \phi}{\partial z} = \frac{1}{\mu_0 V_A \sigma_{\parallel}} \left( \frac{\partial^2 \phi}{\partial x^2} + 2 \frac{\partial E_{xi}}{\partial x} \right) - \frac{\partial \ln(V_A) / \partial x}{\mu_0 V_A \sigma_{\parallel}} \left( \frac{\partial \phi}{\partial x} + 2E_{xi} \right), \text{ at } z = h^{\pm}. \quad (21)$$

Note that all quantities in (21) are evaluated at (or adjacent to) the interface between the magnetosphere and ionosphere at  $z = h$  (or  $z = h^+, h^-$ ) as appropriate. Hence, this is not a differential equation but a constraint upon normal and tangential derivatives at the interface. As such, this provides an alternative boundary condition to the traditional Dirichlet and Neumann conditions.

#### 4. Analytical Solutions

If  $V_A$  does not vary appreciably across the incident Alfvén wave, we may neglect the final term in (21) yielding

$$\frac{\partial \phi}{\partial z} \Big|_{h^-} = \frac{1}{\mu_0 V_A(h^+) \sigma_{\parallel}(x, h^-)} \left( \frac{\partial^2 \phi}{\partial x^2} \Big|_{h^-} + 2 \frac{\partial E_{xi}}{\partial x} \Big|_{h^+} \right), \quad (22)$$

which the remainder of this paper focuses on. Analytical solutions may be found if  $\sigma_p$  and  $\sigma_{\parallel}$  are constant throughout the ionosphere and  $\phi$  is a separable function,  $\phi(x, z) = X(x)Z(z)$ . At the base of the ionosphere we set

$$j_z = 0 \implies \partial \phi / \partial z = 0 \text{ on } z = 0 \quad (23)$$

and assume that the incident Alfvén wave is of the form

$$E_{xi} = E_0 \cos(kx), \quad (24)$$

$k$  being the horizontal (latitudinal) wavenumber.

The solution to (15) with the boundary conditions (22) and (23), subject to (24), is similar to water waves in finite depth water giving

$$\phi = A \sin(kx) \cosh \left( \sqrt{\sigma_p / \sigma_{\parallel}} k z \right) \quad (25)$$

where the coefficient  $A$  is

$$A = \frac{-2E_0}{\mu_0 \sqrt{\sigma_p \sigma_{\parallel}} V_A \sinh \left( \sqrt{\sigma_p / \sigma_{\parallel}} k h \right) + k \cosh \left( \sqrt{\sigma_p / \sigma_{\parallel}} k h \right)}. \quad (26)$$

Together, (25) and (26) define  $\phi$  across the ionosphere  $0 < z < h$  and in certain situations has limiting behavior that permits a simple physical understanding.

If  $\sqrt{\sigma_p/\sigma_{\parallel}}kh \ll 1$ , then  $\phi$  is approximately constant along field lines. In terms of the horizontal wavelength ( $\lambda = 2\pi/k$ ) the requirement is  $\lambda \gg 2\pi\sqrt{\sigma_p/\sigma_{\parallel}}h$ , and the conductivity values quoted earlier give  $\sigma_p/\sigma_{\parallel} \approx 2.5 \times 10^{-4}$ , requiring  $\lambda \gg h/10$ . Taking  $h$  to be 20 km means if  $\lambda \gg 2$  km, the electric field in the ionosphere is essentially independent of altitude and the magnetic field lines are equipotentials.

If the opposite limit holds, then  $\lambda \ll 2\pi\sqrt{\sigma_p/\sigma_{\parallel}}h$  and

$$\phi \approx \frac{A}{2} \sin(kx) \exp\left(\sqrt{\sigma_p/\sigma_{\parallel}}kz\right) \quad (27)$$

in the upper ionosphere. Hence,  $\phi$  (and  $E$ ) decreases exponentially with a scale  $H$ , where

$$H = \frac{1}{k} \sqrt{\frac{\sigma_{\parallel}}{\sigma_p}} = \frac{\lambda}{2\pi} \sqrt{\frac{\sigma_{\parallel}}{\sigma_p}}. \quad (28)$$

#### 4.1. Reflection Coefficients

The reflection properties may be calculated by comparing the ratio of  $E_{xi}$  with the total tangential electric field at the interface, which is also given by  $E_x(x, h^-)$ . In the ionosphere

$$E_x = -\frac{\partial\phi}{\partial x} = -Ak \cos(kx) \cosh\left(\sqrt{\sigma_p/\sigma_{\parallel}}kz\right), \quad (29)$$

and at the interface, after employing (26), this gives

$$E_x^- = \frac{2E_{xi}(x)}{1 + \mu_0\sqrt{\sigma_p\sigma_{\parallel}}(V_A/k) \tanh\left(\sqrt{\sigma_p/\sigma_{\parallel}}kh\right)} \quad (30)$$

(recall  $E_{xi}(x) = E_0 \cos(kx)$ , and  $E_x^- = E_x(x, h^-)$ ).

##### 4.1.1. Full Penetration: $\lambda \gg 2\pi\sqrt{\sigma_p/\sigma_{\parallel}}h$

In this limit the electric field penetrates the ionosphere completely with negligible potential drop along field lines. Approximating

$$\tanh(\alpha) \approx \alpha + \mathcal{O}(\alpha^3) \quad (31)$$

for small  $\alpha$ , we find that (30) gives

$$\frac{E_x^-}{E_{xi}} = \frac{2}{1 + \mu_0\sqrt{\sigma_p\sigma_{\parallel}}(V_A/k)\sqrt{\sigma_p/\sigma_{\parallel}}kh} = \frac{2}{1 + \mu_0 V_A \Sigma_p} = \frac{2}{1 + \Sigma_p/\Sigma_A}, \quad (32)$$

where  $\Sigma_p = \sigma_p h$  and  $\mu_0 V_A = 1/\Sigma_A$ . This is consistent with the result in (13) when  $\sigma_p$  is constant, and we evaluate the integral in (9) noting that  $E_x(x, z) \approx E_x(x, h^+) \equiv E_x^+$  in this limit (and  $E_x^+ = E_x^-$  since the tangential electric field is continuous).

##### 4.1.2. Partial Penetration: $\lambda \ll 2\pi\sqrt{\sigma_p/\sigma_{\parallel}}h$

In this limit, (27) indicates that we have an evanescent solution with  $E_x \propto \exp(z/H)$  and the skin depth  $H$  given in (28). Approximating the tanh function in equation (30) by its asymptotic value of 1 gives

$$\frac{E_x^-}{E_{xi}} = \frac{2}{1 + \mu_0\sqrt{\sigma_p\sigma_{\parallel}}V_A [H\sqrt{\sigma_p/\sigma_{\parallel}}]} = \frac{2}{1 + \mu_0 V_A \sigma_p H} = \frac{2}{1 + \sigma_p H/\Sigma_A}, \quad (33)$$

where the square-bracketed term above is equal to  $1/k$  and has been reexpressed using (28). The final result in (33) is also consistent with the result in (13) when we note that  $\Sigma_p$  in (9) is simply the integral of  $\exp(-z/H)$

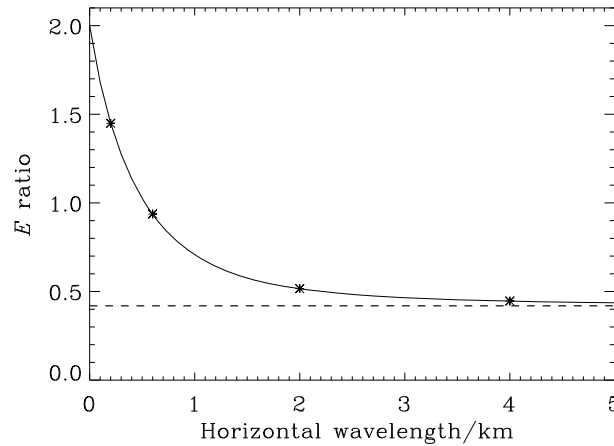


**Figure 2.** The ratio of the total electric field  $E_x^+ = E_x(x, h^+)$  at the base of the magnetosphere to  $E_{xi}$  (the incident electric field) as a function of horizontal wavelength. The solid line is the analytical result (equation (34)), and the symbols are from numerical results using the boundary condition (22). ( $\sigma_p = 5 \times 10^{-4}$  mho/m,  $\sigma_{||} = 2$  mho/m,  $V_A = 3 \times 10^5$  ms $^{-1}$ , and  $h = 20$  km.)

from 0 to  $h$  with  $\sigma_p$  constant giving  $\Sigma_p = \sigma_p H$  to leading order (when we note  $\lambda \ll 2\pi\sqrt{\sigma_p/\sigma_{||}} \Rightarrow H/h \ll 1$ ).

The agreement in the above limits of our solutions with the standard results gives confidence in the utility of our novel boundary condition (22) which we will now use to validate a numerical solution for a variety of wavelengths (besides the limits considered above) before considering more general incident Alfvén wave profiles and conductivity distributions.

## 5. Numerical Solutions

The elliptic equation (15) was solved subject to the boundary conditions (22) and (23) using the Successive Over-Relaxation method. Typically, the scheme was iterated until the potential had converged to better than 0.1%. The algorithm typically takes longer to converge than when a Dirichlet condition is imposed at  $z = h^-$ , and it is important to optimize the relaxation parameter. Although the scheme can accommodate general  $\sigma_p(x, z)$  and  $\sigma_{||}(x, z)$ , we begin with results that assume uniform  $\sigma_p$ ,  $\sigma_{||}$  and  $V_A$  to allow validation with the analytical solution in (25) and to gain some insight into the nature and role of the terms in the interface condition (22).

converge than when a Dirichlet condition is imposed at  $z = h^-$ , and it is important to optimize the relaxation parameter. Although the scheme can accommodate general  $\sigma_p(x, z)$  and  $\sigma_{||}(x, z)$ , we begin with results that assume uniform  $\sigma_p$ ,  $\sigma_{||}$  and  $V_A$  to allow validation with the analytical solution in (25) and to gain some insight into the nature and role of the terms in the interface condition (22).

### 5.1. Single Fourier Mode

The results in this subsection have an  $x$  domain of extent  $\lambda/2$  and imposed  $\phi(x = 0, z) = \phi(x = \lambda/2, z) = 0$ . These boundary conditions allow us to consider a single Fourier mode (or horizontal wavelength) by choosing  $E_{xi}$  of the form in (24), which will permit a detailed comparison with analytical solutions. The  $z$  domain was chosen to represent the  $E$  region and spanned 20 km. A grid of  $100 \times 100$  points was employed.

To validate the numerical solution, we adopted typical daytime parameters ( $\sigma_p = 5 \times 10^{-4}$  mho/m,  $\sigma_{||} = 2$  mho/m,  $V_A = 3 \times 10^5$  ms $^{-1}$ ) and chose  $E_{xi} = E_0 \cos(2\pi x/\lambda)$  for a variety of wavelengths  $\lambda$ . Equation (30) gives the ratio of total  $E_x$  at the interface to  $E_{xi}$  as

$$\frac{E_x(x, h)}{E_{xi}(x)} = \frac{2}{1 + \mu_0 V_A \sqrt{\sigma_p \sigma_{||}} (\lambda/2\pi) \tanh(\sqrt{\sigma_p/\sigma_{||}} 2\pi h/\lambda)}. \quad (34)$$

Figure 2 shows the ratio given above as a function of wavelength as the solid line. The asterisks represent numerical results from separate runs with  $\lambda = 0.2, 0.6, 2.0$ , and  $4$  km. The dashed line at  $E_x/E_{xi} = 0.419$  is the large  $\lambda$  limit based upon (32) to which the numerical results asymptote. Indeed, a run with  $\lambda = 20$  km (not plotted) had a ratio of 0.4203 and is in excellent agreement with the value expected from the analytical formula of 0.4204, thus confirming the accuracy of the numerical solution and clearly tending to the limiting value.

The form of the potential given in (25) indicates that  $\phi$  has its maximum magnitude at  $x = \lambda/4$  and varies with  $z$  as  $\cosh(\sqrt{\sigma_p/\sigma_{||}} 2\pi h/\lambda)$ ; Figure 3 shows this variation by plotting  $\phi(x = \lambda/4, z)/\phi_0$  with  $z$ , where  $\phi_0 = \phi(x = \lambda/4, h^-)$ . The solid lines are numerical solutions for horizontal wavelengths of  $\lambda = 0.2, 0.6, 2, 4$ , and  $20$  km, and the symbols represent values based upon the analytical solution in (25). Once again, the agreement of analytical and numerical values is to within the accuracy of convergence set on the iterative scheme. Figure 3 clearly shows the expected large wavelength ( $\lambda \gg 2$  km) equipotential solution (see the  $\lambda = 20$  km case) where  $\phi$  is constant along field lines. The smooth transition to the small wavelength ( $\lambda \ll 2$  km) limit with a clear evanescent behavior at the top of the ionosphere is also evident. In this regime the skin depth  $H = (\lambda/2\pi)\sqrt{\sigma_{||}/\sigma_p}$  suggests a decay length of  $2$  km and  $6$  km for the  $\lambda = 0.2$  and  $0.6$  km cases for the parameters chosen. Note also that all cases in Figure 3 have  $\partial\phi/\partial z|_{z=0} = 0$  consistent with  $j_z(x, z = 0) = 0$ .

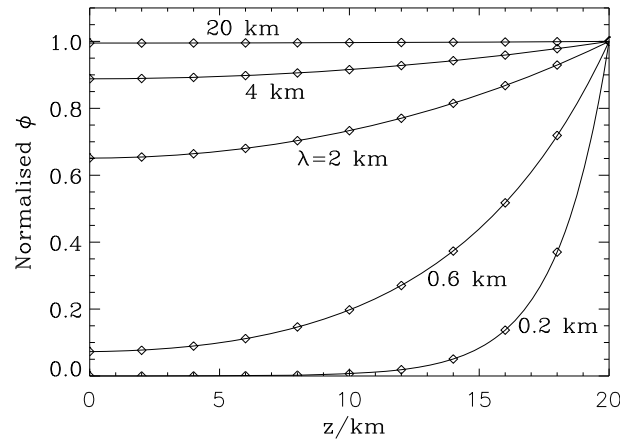


**Figure 3.** The variation of  $\phi$  with altitude across the ionosphere (normalized by the value at  $z = h^-$ ). Results are shown for horizontal wavelengths of 0.2, 0.6, 2, 4, and 20 km. The solid lines are numerical results, and the symbols represent the analytical solution (25) which varies as  $\cosh\left(\sqrt{\sigma_p/\sigma_{\parallel}}2\pi h/\lambda\right)$ . (Parameters are the same as Figure 2.)

### 5.1.1. Interface Condition-Dominant Terms

The boundary condition (22) comprises three terms, and in certain limits, one of these may be neglected, resulting in an approximate form that may permit physical insights or interpretations.

We begin by recognizing that the analytical result in (25) can be written as follows:

$$\phi(x, z) = \phi_0 \sin(x/\lambda) \cosh(z/H) / \cosh(h/H), \quad (35)$$

so  $\phi$  is characterized by two length scales,  $\lambda$  and  $H$ , in the  $x$  and  $z$  directions, respectively. (Here  $\lambda = \lambda/2\pi$ .) Thus,  $E_x$  and  $E_z$  may be determined from (6) and the requirement  $\nabla \cdot \mathbf{j} = 0$  becomes (on using (5))

$$\sigma_p/\lambda^2 = \sigma_{\parallel}/H^2, \quad (36)$$

which determines the relation between the two scale lengths, consistent with (28).

We also note that once  $E_x$  has been determined from (6) and (35), it is possible to calculate  $\Sigma_p(x)$  as defined in (9) analytically. Since  $\sigma_p$  is constant in this particular solution, we find

$$\Sigma_p = \sigma_p H \tanh(h/H) \equiv \lambda \sqrt{\sigma_p \sigma_{\parallel}} \tanh\left(\sqrt{\sigma_p/\sigma_{\parallel}} h/\lambda\right) \quad (37)$$

after (36) has been used. This result is quite general and includes the fully penetrative limit (section 4.1.1) in which  $\lambda \gg 2\pi\sqrt{\sigma_p/\sigma_{\parallel}}h \Rightarrow H \gg h$  and  $\tanh(h/H) \approx h/H$  meaning (37) reduces to  $\Sigma_p \approx \sigma_p h$ . In the opposite limit of a strongly evanescent solution (section 4.1.2),  $\lambda \ll 2\pi\sqrt{\sigma_p/\sigma_{\parallel}}h \Rightarrow H \ll h$  and  $\tanh(h/H) \approx 1$  meaning (37) reduces to  $\Sigma_p \approx \sigma_p H$ . These conductance limits were also noted in sections 4.1.1 and 4.1.2. The expression for  $\Sigma_p$  in (37) has the advantage that it is valid quite generally for large, small, and intermediate wavelengths with their associated varying degrees of penetration and  $\Sigma_p$ . Indeed, using (37), we can rewrite the denominator in (30) and (34) as  $1 + \Sigma_p/\Sigma_A$  which recovers agreement with (13) for arbitrary  $\lambda$ .

#### 5.1.1.1. Insulating Ionosphere

In the limit where the term on the left-hand side of (22) may be neglected compared to the first term on the right, we have

$$\frac{\phi_0}{H} \tanh\left(\frac{h}{H}\right) \ll \frac{\phi_0}{\mu_0 V_A \sigma_{\parallel} \lambda^2} \equiv \frac{\phi_0}{\mu_0 V_A \sigma_p H^2}, \quad (38)$$

where (35) and (36) have been employed. Using (37) to introduce  $\Sigma_p$ , we find

$$\mu_0 V_A \Sigma_p \ll 1. \quad (39)$$

This result holds for arbitrary  $\lambda$  and is associated solely with the neglect of the term on the left-hand side of (22). The remaining terms in (22) balance to give

$$\frac{1}{\mu_0 V_A \sigma_{\parallel}} \left( -\frac{\partial E_x}{\partial x} + 2 \frac{\partial E_{xi}}{\partial x} \right) \approx 0 \text{ on } z = h \quad (40)$$

after substituting  $-\partial\phi/\partial x = E_x$ , the  $x$  component of the total electric field. The solution to (40) is simply  $E_x \approx 2E_{xi}$ , and since  $E_x$  is also equal to  $E_{xi} + E_{xr}$ , we conclude  $E_{xr} \approx E_{xi}$  which is exactly as expected for a highly reflecting insulator.



### 5.1.1.2. Conducting Ionosphere

If the first term on the right-hand side of (22) is negligible compared to the term on the left-hand side, we have the opposite inequality to that in (38) which we choose to write (on employing (36)) in the form

$$\begin{aligned} \mu_0 V_A \sigma_p H \tanh(h/H) &\gg 1, \\ \text{or equivalently, } \mu_0 V_A \Sigma_p &\gg 1. \end{aligned} \quad (41)$$

This expression indicates reflection from a highly conducting ionosphere and is valid for arbitrary  $\lambda$  since  $\Sigma_p$  is given by the general expression in (37).

In (22) the left-hand side term and the second term on the right-hand side must now balance, giving the leading approximation as

$$\frac{\phi_0}{H} \tanh(h/H) \approx \frac{-2}{\mu_0 V_A \sigma_{\parallel}} \frac{E_0}{\lambda}, \quad (42)$$

where (24) has been employed. Multiplying through by  $\cos(x/\lambda)$  and noting that  $E_x(x, h^-) = -\partial\phi(x, h^-)/\partial x = -(\phi_0/\lambda) \cos(x/\lambda)$  leads to

$$\frac{E_x(x, h)}{H} \tanh(h/H) \approx \frac{2E_{xi}}{\mu_0 V_A \sigma_{\parallel} \lambda^2}, \quad (43)$$

which may be reformulated using (36) as

$$\left. \frac{E_x}{E_{xi}} \right|_{(x,h)} \approx \frac{2 \coth(h/H)}{\mu_0 V_A \sigma_p H}. \quad (44)$$

Employing (37) to introduce the general  $\Sigma_p$  expression gives

$$\left. \frac{E_x}{E_{xi}} \right|_{(x,h)} \approx \frac{2}{\mu_0 V_A \Sigma_p} \ll 1, \quad (45)$$

which is valid for arbitrary penetration of the ionosphere by the electric field (i.e., arbitrary  $h/H$ ). Note that this result is consistent with (13) given that the limit  $\Sigma_p/\Sigma_A \gg 1$  applies here, as shown in (41), and we conclude  $E_x/E_{xi} \rightarrow 0$  as  $\mu_0 V_A \Sigma_p \rightarrow \infty$ . Hence,  $E_{xi} \approx -E_x$  (to give  $E_x = E_{xi} + E_{xr} \ll E_{xi}$ ), and we recover the expected phase relation for the reflected Alfvén wave in the limit of a perfect conductor.

### 5.1.1.3. Undriven Ionosphere

The above subsections have shown how the dominance of the two terms on the right-hand side of (22) corresponds to an insulating ionosphere, while the dominance of the term on the left-hand side and the final term on the right-hand side to a highly conducting ionosphere. For intermediate cases, all three terms must be retained. Finally, the neglect of the second term on the right-hand side of (22) means that there is no incident wave, and the trivial solution results: Balancing the other two terms gives

$$\begin{aligned} \phi_0 \times [\tanh(h/H) \mu_0 V_A \sigma_{\parallel} \lambda^2 / H + 1] &= 0, \\ \text{or } \phi_0 \times [\mu_0 V_A \sqrt{\sigma_p \sigma_{\parallel}} \lambda \tanh(\sqrt{\sigma_p / \sigma_{\parallel}} h / \lambda) + 1] &= 0. \end{aligned} \quad (46)$$

Since  $\lambda$  may be chosen arbitrarily, the only way (46) is generally satisfied is if  $\phi_0 = 0$ . It may be thought that there is a special value of  $\lambda$  for which the square bracket in (46) is zero; however, a little thought shows that the bracket never vanishes for real  $\lambda$  as the first term in the bracket is always positive. Moreover, setting the contents of the bracket to zero requires  $\Sigma_p/\Sigma_A = -1$  which is not a physically realistic solution. This is not surprising as the neglect of the third term in (22) means that there is no incident wave to drive the system, and we are required to adopt the trivial solution  $\phi_0 = 0$ .

### 5.1.2. Conductivity Jump

One further analytical result, which has nonuniform conductivities, can be derived if we assume that there is a step in  $\sigma_{\parallel}$  and/or  $\sigma_p$  at  $z = z_s$ . We assume that these conductivities are independent of  $x$  and have constant value on either side of the step. While we do not advocate this as a realistic model of the ionosphere, it could provide a simple way of investigating regions where the conductivities change over a small vertical range (e.g.,  $\sigma_p$  from the  $E$  to the  $F$  region or the dramatic decrease in  $\sigma_{\parallel}$  over the  $E$  region.). The main purpose of deriving the solution here is to validate the numerical solution.



Integration of the governing elliptic equation (15) across a vanishingly small height straddling the discontinuity (from  $z_s^-$  to  $z_s^+$ ) yields

$$\left[ \sigma_{\parallel} \frac{\partial \phi}{\partial z} \right]_{z_s^-}^{z_s^+} = 0, \quad (47)$$

i.e.,  $\sigma_{\parallel} \partial \phi / \partial z (= -j_z)$  is continuous across the step. More generally, we can write the solution to (47) as  $\partial \phi / \partial z = f(z) / \sigma_{\parallel}(z)$ , where  $f(z)$  is a continuous function. Further integration of the latter equation across the step gives

$$[\phi]_{z_s^-}^{z_s^+} = 0, \quad (48)$$

so  $\phi$  is also continuous across the step.

For the remainder of this derivation, we assume a separable single Fourier mode for the incident wave of the form (24) requiring

$$\phi = Z(z) \sin(kx). \quad (49)$$

The continuity relations (47) and (48) then become, in terms of  $Z$ ,

$$\left[ \sigma_{\parallel} \frac{\partial Z}{\partial z} \right]_{z_s^-}^{z_s^+} = 0 \quad \text{and} \quad [Z]_{z_s^-}^{z_s^+} = 0. \quad (50)$$

Away from the step in conductivities (where the conductivities are uniform), the governing elliptic equation (15) reduces to

$$\frac{d^2 Z}{dz^2} - k^2 \frac{\sigma_p}{\sigma_{\parallel}} Z = 0 \quad (51)$$

which is an ordinary differential equation in  $z$ . The solution has a local wavenumber (or inverse decay length) of

$$\kappa = k \sqrt{\sigma_p / \sigma_{\parallel}} \quad (52)$$

which will vary with  $z$  since  $\sigma_p$  and  $\sigma_{\parallel}$  change at  $z_s$ . The values of  $\kappa$  on either side of  $z_s$  are defined as

$$\kappa(z) = \begin{cases} \kappa^- = k \sqrt{\sigma_p^- / \sigma_{\parallel}^-}, & 0 < z < z_s \\ \kappa^+ = k \sqrt{\sigma_p^+ / \sigma_{\parallel}^+}, & z_s < z < h \end{cases} \quad (53)$$

in terms of the conductivities above (+) and below (−)  $z_s$ . The solution for  $Z$  (and hence  $\phi$ ) over the entire ionosphere is found by solving (50) in the region  $0 < z < z_s$  subject to the boundary condition at  $z = 0$ , then matching across the discontinuity at  $z = z_s$  to the solution of (50) in the region  $z_s < z < h$ . The boundary condition  $\partial \phi / \partial z = 0$  (i.e.,  $\partial Z / \partial z = 0$ ) at  $z = 0$  determines the lower solution as

$$Z = c_0 \cosh(\kappa^- z), \quad 0 < z < z_s, \quad (54)$$

where  $c_0$  is a constant. Hence, the expressions in (50) at  $z_s^-$  are

$$\begin{aligned} Z(z_s^-) &= c_0 \cosh(\kappa^- z_s), \\ \left( \sigma_{\parallel} \frac{\partial Z}{\partial z} \right)_{z_s^-} &= c_0 k \sqrt{\sigma_p^- \sigma_{\parallel}^-} \sinh(\kappa^- z_s). \end{aligned} \quad (55)$$

Over the upper region ( $z_s < z < h$ ), we have the general solution (with constants  $c_1$  and  $c_2$ )

$$Z = c_1 \cosh(\kappa^+ z) + c_2 \sinh(\kappa^+ z), \quad z_s < z < h, \quad (56)$$

and evaluating the terms needed in (50) at  $z_s^+$  gives

$$\begin{aligned} Z(z_s^+) &= c_1 \cosh(\kappa^+ z_s) + c_2 \sinh(\kappa^+ z_s), \\ \left( \sigma_{\parallel} \frac{\partial Z}{\partial z} \right)_{z_s^+} &= c_1 k \sqrt{\sigma_p^+ \sigma_{\parallel}^+} \sinh(\kappa^+ z_s) + c_2 k \sqrt{\sigma_p^+ \sigma_{\parallel}^+} \cosh(\kappa^+ z_s). \end{aligned} \quad (57)$$

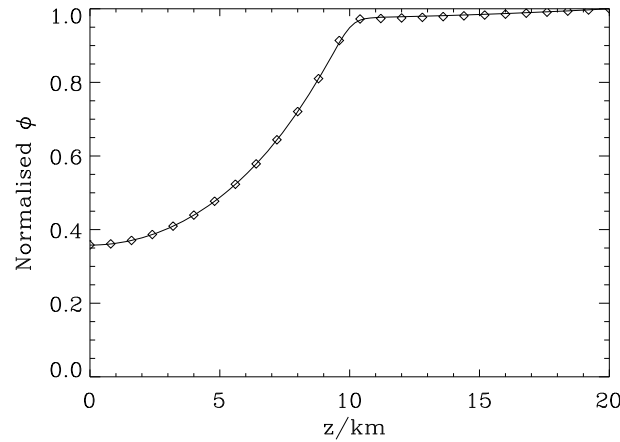


**Figure 4.** A similar format plot to Figure 3, except that  $\sigma_{\parallel}$  jumps from a value of 0.02 mho/m ( $0 < z < 10$  km) to 2 mho/m ( $10 < z < 20$  km). The horizontal wavelength is 2 km. Other parameters are the same as used in Figure 2.

Using the continuity properties, (49) allows the expressions in (55) and (57) to determine  $c_1$  and  $c_2$  in terms of the arbitrary amplitude  $c_0$ . After a little algebra, we find

$$\begin{aligned} c_1/c_0 &= \cosh(\kappa^- z_s) \cosh(\kappa^+ z_s) \\ &\quad - \sqrt{\sigma_p^- \sigma_{\parallel}^- / \sigma_p^+ \sigma_{\parallel}^+} \sinh(\kappa^- z_s) \sinh(\kappa^+ z_s), \\ c_2/c_0 &= \sqrt{\sigma_p^- \sigma_{\parallel}^- / \sigma_p^+ \sigma_{\parallel}^+} \sinh(\kappa^- z_s) \cosh(\kappa^+ z_s) \\ &\quad - \cosh(\kappa^- z_s) \sinh(\kappa^+ z_s), \end{aligned} \quad (58)$$

which completes the determination of  $\phi$  in (49) using (54), (56), and (58). Figure 4 shows an example for  $z_s = 10$  km with a jump in  $\sigma_{\parallel}$  from 0.02 to 2.0 mho/m ( $\sigma_p$  has no jump) and plots the normalized  $\phi$  with altitude for  $\lambda = 2$  km. The numerical results (solid line) and analytical solution (54) and (56) are clearly in good agreement. Note that the

numerical solution actually allowed  $\sigma_{\parallel}$  to change continuously over a narrow layer centered on  $z = z_s$  so that finite differencing could be used reliably. Hence, we cannot compare the analytical and numerical solutions quantitatively for this example, although the qualitative agreement is evident. Other examples (not shown here) confirm agreement when both  $\sigma_{\parallel}$  and  $\sigma_p$  have a jump at  $z = z_s$ .

## 5.2. Numerical Checks

The use of a more general conductivity distribution soon leads us to not having an exact analytical solution to compare with. This is equally true of more general incident Alfvén waves  $E_{xi}(x)$  than the sinusoidal form assumed in section 5.1. However, there are other checks we can apply to the numerical solution to confirm its accuracy and validity besides iterating until  $\phi$  has been determined to a chosen accuracy.

### 5.2.1. Current Continuity

Since we assume  $\nabla \cdot \mathbf{j} = 0$ , Gauss' theorem requires that there is no net current flow across the boundaries of the 2-D ( $x, z$ ) domain. A simple integration of the normal current component over these boundaries (compared to the integral of the modulus of the normal component) shows that  $\nabla \cdot \mathbf{j} = 0$  was always met to better than 1%.

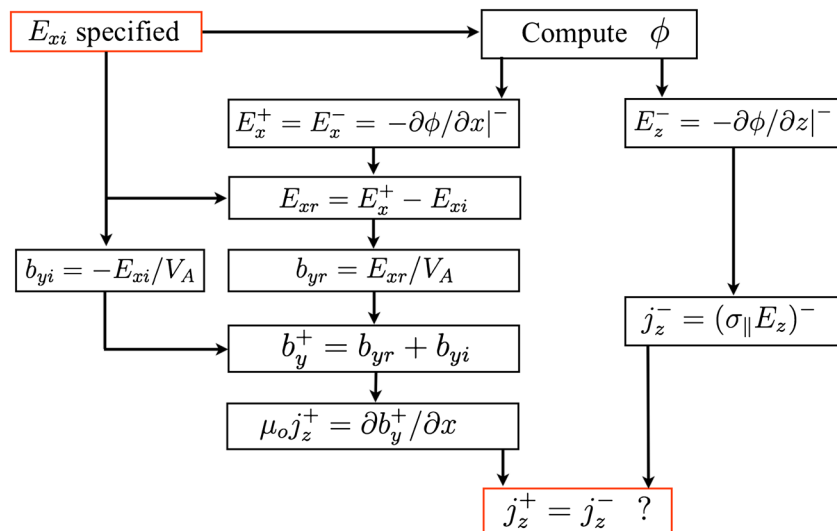


**Figure 5.** Flow chart outlining the current consistency check. Given the incident wave ( $E_{xi}$ ), there are two routes to calculate  $j_z$  at the interface: one through the magnetosphere ( $j_z^+$ ) and the other through the ionosphere ( $j_z^-$ ). For an accurate self-consistent solution, these will be the same to within the accuracy of the solution.

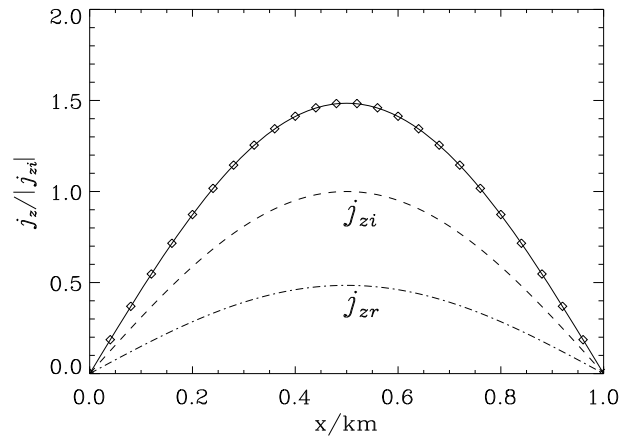


**Figure 6.** The variation field-aligned current at the magnetosphere-ionosphere interface with  $x$  for  $\lambda = 2$  km. The solid line is  $j_z^-$ , and the symbols are  $j_z^+$ . (Other parameters are the same as in Figure 2.)

$z = h^-$  allows the determination of  $E_x^- = E_x(x, z = h^-)$ , which is equal to  $E_x^+$  (at  $z = h^+$ ) since  $E_x$  is continuous at  $z = h$ . Once the total electric field at the base of the magnetosphere ( $E_x^+$ ) is known, we may deduce  $E_{xr}$  (the reflected Alfvén wave field) using (4) and the reflected magnetic field ( $b_{yr}$ ) using (3). Hence, the total Alfvén wave magnetic field at  $z = h^+$  is known (from (4)), and  $j_z^+$  then follows from Ampère's Law. Since  $j_z$  is continuous across the interface, we shall require  $j_z^+ = j_z^-$ .

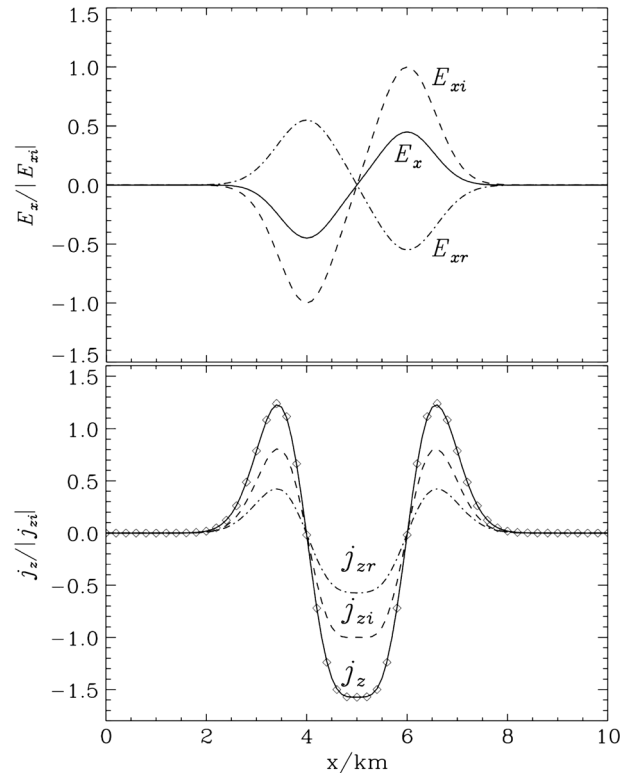


**Figure 7.** The variation of (top)  $E_x$  and (bottom)  $j_z$  at the magnetosphere-ionosphere interface ( $z = h$ ) with  $x$ . The total  $j_z$  consists of a strong downward current that closes in two adjacent smaller upward currents. Both  $j_z^+$  (symbols) and  $j_z^-$  (solid line) are shown. Parameters are the same as in Figure 2.

### 5.2.2. Current Consistency

The route through which the numerical solution is determined allows for two expressions for  $j_z$  at the interface to be derived. If the potential is indeed the self-consistent solution for the given incident Alfvén wave, then these expressions should be the same. Figure 5 outlines the strategy of the test.

Given  $E_{xi}$  (the incident Alfvén wave electric field), it immediately follows that we know  $b_{yi}$  from equation (3). Also, given  $E_{xi}$ , we can specify the interface condition ((21) or (22)) and hence solve for  $\phi$  in the ionosphere. If  $\phi$  is known, then (6) gives  $E_x$  and  $E_z$  throughout the ionosphere. Evaluating  $E_z$  at  $z = h^-$  (and using  $\sigma_{||}$ ) determines  $j_z$  there too (i.e.,  $j_z^-$ ).

Alternatively, evaluating  $E_x = -\partial\phi/\partial x$  at

Figure 6 shows the variation of  $j_z(x, z = h)$  for the  $\lambda = 2$  km case studied previously in Figures 2 and 3. The solid line shows  $j_z^-$  (based upon  $-\sigma_{||}\partial\phi/\partial z$  at  $z = h^-$ ), and the diamonds represent  $j_z^+$  at  $z = h^+$  (based upon the magnetospheric Alfvén wave solution). The discrepancy between the two currents does not exceed 0.1%. Also shown are the currents in the incident and reflected Alfvén waves, the sum of which is  $j_z^+$ .

### 5.3. General Numerical Results

Having established the reliability of the numerical solution and boundary condition, we now consider cases which are relevant to magnetosphere-ionosphere coupling but do not have an analytical solution. We begin by considering an isolated current system as shown in Figure 7 driven by a bipolar Alfvén wave ( $E_{xi}$ ) that is incident upon an ionosphere with uniform conductivities ( $\sigma_p = 5 \times 10^{-4}$  mho/m,  $\sigma_{||} = 2$  mho/m,  $V_A = 3 \times 10^5$  m/s,  $h = 20$  km and a grid with  $200 \times 200$  points was used). For the parameters chosen the ionosphere is a good conductor, and the reflected electric field ( $E_{xr}$ ) has the opposite phase to  $E_{xi}$ . Figure 7 (bottom) shows the field-aligned currents, with the incident and reflected currents having the same phase—as expected when the ionosphere is a good conductor. The

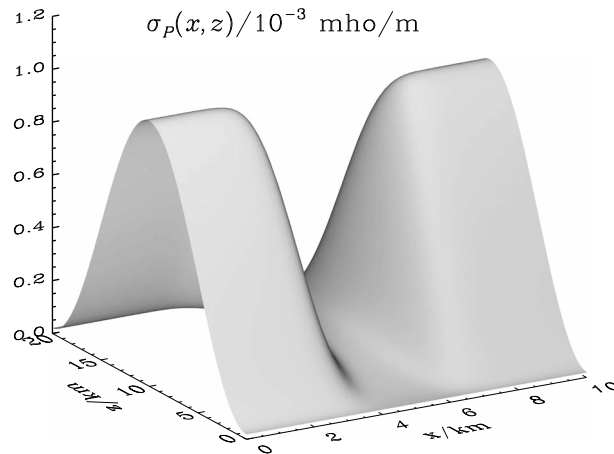


**Figure 8.** A surface plot of nonuniform  $\sigma_p(x, z)$  with conductivity depleted below the downward current. In the undepleted regions, the height-integrated Pedersen conductivity is similar to that employed in constructing the results shown in Figure 7.

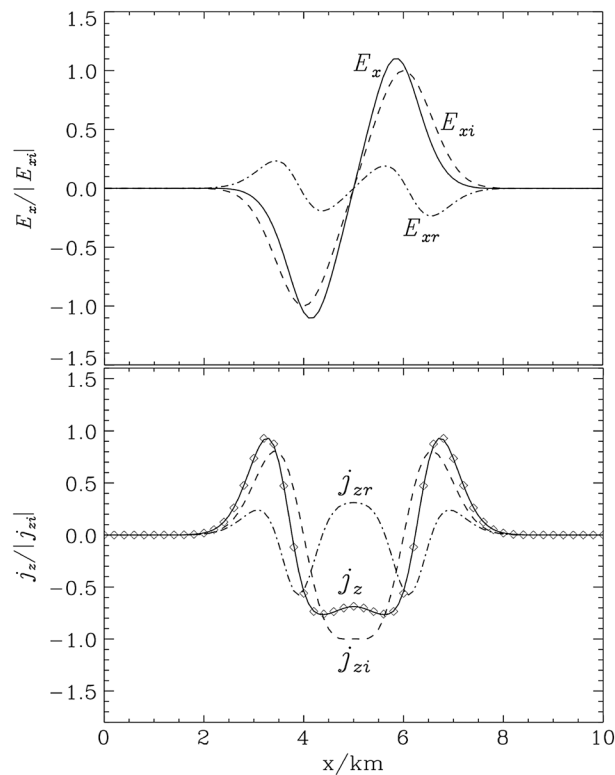


**Figure 9.** A similar format to Figure 7. The incident Alfvén wave and parameters used to generate the results in Figures 7 and 9 are the same except that Figure 9 used the  $\sigma_p$  distribution displayed in Figure 8, while Figure 7 used a uniform  $\sigma_p$  of  $5 \times 10^{-4}$  mho/m. Note how the reflected fields over the downward current region ( $4 < x < 6$  km) differ between Figures 7 and 9, and hence, the total  $E_x$  and  $j_z$  are also modified there.

upward-downward-upward current structure is similar to that used by *Karlsson and Marklund* [1998] and thought to correspond to the observations reported by, e.g., *Streltsov and Marklund* [2006], *Streltsov and Karlsson* [2008], *Marklund et al.* [2001], and *Michell et al.* [2008].

It is known that strong downward currents can significantly deplete the ionosphere of electrons and change the conductivity as in the nonresponsive magnetosphere driving addressed by *Blixt and Brekke* [1996], *Doe et al.* [1995], *Karlsson and Marklund* [1998], and *Zettergren and Semeter* [2012], as well as for the responsive magnetospheric driving of a sheet ionosphere considered by *Lysak and Song* [2002], *Cran-McGreehin et al.* [2007], and *Russell et al.* [2010]. A future paper will study the nonlinear self-consistent evolution of a resolved ionosphere with responsive magnetospheric driving in which the ionospheric conductivity is modified by current closure. The focus of the present paper, however, is to establish the validity and practical solution of the potential problem with the responsive boundary condition in (22). For the moment we shall simply define a depleted ionosphere that is typical of that associated with downward currents, calculate the associated conductivity, and then test our method of solution using these conductivity profiles.

Figure 8 shows  $\sigma_p(x, z)$  and has been chosen such that in the undepleted regions ( $x < 3$  km and  $x > 7$  km) the height-integrated  $\sigma_p$  is approximately the same as used for generating the results shown in Figure 7.

Figure 9 displays the electric fields and field-aligned currents in the same format used in Figure 7. All parameters, including the incident wave profile ( $E_{xi}$ ), are unchanged from those used in generating Figure 7, except that  $\sigma_p$  has the distribution displayed in Figure 8. Note how in the undepleted region ( $x < 3$  km and  $x > 7$  km) the electric field and current profiles are similar to in Figure 7 and exhibit reflection from a good conductor. Over the central region ( $4 < x < 6$  km),  $\sigma_p$  has been reduced by a factor of about

10, and the solution there is now more representative of reflection from an insulator:  $E_{xi}$  and  $E_{xr}$  are in phase, while  $j_{zi}$  and  $j_{zr}$  are out of phase. The diamond symbols in Figures 7 and 9 again depict  $j_z^+$  being in good agreement with  $j_z^-$  shown by the solid line.

## 6. Responsive Magnetospheric Driver

The response of the magnetosphere to changing ionospheric structure via the boundary condition (22) may be appreciated by comparing with the situation that results from nonresponsive boundary conditions. The latter case has been implemented elsewhere previously by applying Dirichlet or Neumann boundary conditions which impose either the total potential or the total field-aligned current on the interface, respectively [Doe et al., 1995; Karlsson and Marklund, 1998; Zettergren and Semeter, 2012]. In these models, the ionosphere may become depleted and the conductivities modified, but the total potential (or field-aligned current) on the interface which represents the magnetospheric driving remains unchanged, and so the magnetospheric potential (or current) solution is fixed and unresponsive.

Figures 7 and 9 show how the boundary condition (22) can be interpreted as providing a self-consistent responsive magnetospheric solution. Both sets of results in these figures have the same incident Alfvén wave described by  $E_{xi}$  and  $j_{zi}$  which could be set up by processes in the distant magnetosphere. The solution in the magnetosphere is a sum of incident and reflected Alfvén waves. Since the reflected wave is modified by the ionospheric conductivity, the resulting total magnetospheric solution is modified also. This is readily seen by comparing the total  $E_x$  and  $j_z$  (solid lines) in Figures 7 and 9. In the undepleted case (Figure 7), the bipolar total  $E_x$  has a normalized amplitude of about 0.45, whereas in the depleted case (Figure 9) it is about 1.1. Similarly, the shape of the total current changes between these two cases, as does the size of the downward current from 1.6 (depleted) to 0.8 (undepleted). The adjustment of both the total magnetospheric electric field ( $E_x^+$ ) and current ( $j_z^+$ ) to the changing conductivity means that the boundary condition (22) represents a responsive magnetosphere.

## 7. Discussion and Conclusion

We have derived and tested a novel boundary condition that can be imposed at the top of a distributed ionosphere to represent a responsive magnetosphere. Careful testing against analytical solutions and conserved quantities has established its validity. Future studies could explore alternative numerical methods for solving the elliptical potential problem as they may be more efficient than Successive Over-Relaxation.

An important future development will be the introduction of a responsive ionosphere where the current flow in the ionosphere redistributes electrons and ions according to continuity equations. When used in conjunction with the responsive magnetosphere boundary condition developed here, the fully self-consistent coupled system may exhibit nonlinear behavior such as steepening and the formation of small scales. This has been shown to be the case for when the simplification of a sheet ionosphere is adopted with a responsive magnetosphere boundary condition [Cran-McGreehin et al., 2007]. (If Dirichlet or Neumann boundary conditions are adopted, steepening is not seen to occur.)

Future work will investigate whether the steepening process still operates efficiently in a distributed ionosphere model. If small spatial scales can be produced by this process, it may lead to electron inertial terms becoming important [Russell et al., 2013], which are often invoked to interpret observations [Semeter and Blixt, 2006], even when the initial equilibrium and incident Alfvén wave do not contain any small scales.

## References

- Blixt, E. M., and A. Brekke (1996), A model of currents and electric fields in a discrete auroral arc, *Geophys. Res. Lett.*, **23**(18), 2553–2556.
- Cran-McGreehin, A. P., A. N. Wright, and A. W. Hood (2007), Ionospheric depletion in auroral downward currents, *J. Geophys. Res.*, **112**, A10309, doi:10.1029/2007JA012350.
- Doe, R. A., J. F. Vickrey, and M. Mendillo (1995), Electrodynamical model for the formation of auroral ionospheric cavities, *J. Geophys. Res.*, **100**(A6), 9683–9696.
- Karlsson, T., and G. Marklund (1998), Simulations of effects of small-scale auroral current closure in the return current region, in *Phys. Space Plasmas*, vol. 15, edited by T. Chang and J. R. Jasperse, pp. 401–406, MIT Center for Theoretical Geo/Cosmo Plasma Physics, Cambridge, Mass.
- Kelley, M. C. (2009), *The Earth's Ionosphere*, 2nd ed., International Geophys. Ser., vol. 96, Academic Press, London, U. K.
- Lysak, R. L., and Y. Song (2002), Energetics of the ionospheric feedback interaction, *J. Geophys. Res.*, **107**(A8), 1160, doi:10.1029/2001JA000308.

### Acknowledgments

The authors are grateful to the International Space Science Institute (ISSI, Bern, Switzerland) for sponsoring a series of international workshops through which the work in this paper was undertaken. We also thank the referees for their comments—particularly Evgeny Fedorov (whose suggestions improved section 5.1.1). A.J.B.R. thanks STFC for present support through consolidated grant ST/K000993/1 and gratefully acknowledges a Royal Commission for the Exhibition of 1851 Research Fellowship that also assisted this work.

Alan Rodger thanks Evgeny Fedorov and an anonymous reviewer for their assistance in evaluating this paper.

- Marklund, G. T., et al. (2001), Temporal evolution of the electric field accelerating electrons away from the auroral ionosphere, *Nature*, *414*, 724–727.
- Michell, R. G., K. A. Lynch, and H. C. Stenbaek-Nielsen (2008), Ground-based observational signature of a downward current channel in an active auroral arc, *Geophys. Res. Lett.*, *35*, L08101, doi:10.1029/2008GL033596.
- Rees, M. H. (1989), *Physics and Chemistry of the Upper Atmosphere*, Cambridge Univ. Press, Cambridge, U. K.
- Russell, A. J. B., and A. N. Wright (2012), Magnetosphere-ionosphere waves, *J. Geophys. Res.*, *117*, A01202, doi:10.1029/2011JA016950.
- Russell, A. J. B., A. N. Wright, and A. W. Hood (2010), Self-consistent ionospheric plasma density modifications by field-aligned currents: Steady state solutions, *J. Geophys. Res.*, *115*, A04216, doi:10.1029/2009JA014836.
- Russell, A. J. B., A. N. Wright, and A. V. Streltsov (2013), Production of small-scale Alfvén waves by ionospheric depletion, nonlinear magnetosphere-ionosphere coupling and phase mixing, *J. Geophys. Res. Space Physics*, *118*, 1450–1460, doi:10.1002/jgra.50168.
- Semeter, J., and E. M. Blixt (2006), Evidence for Alfvén wave dispersion identified in high resolution auroral imagery, *Geophys. Res. Lett.*, *33*, L13106, doi:10.1029/2006GL026274.
- Streltsov, A. V., and T. Karlsson (2008), Small-scale, localized electromagnetic waves observed by Cluster: Result of magnetosphere-ionosphere interactions, *Geophys. Res. Lett.*, *35*, L22107, doi:10.1029/2008GL035956.
- Streltsov, A., and G. T. Marklund (2006), Divergent electric fields in downward current channels, *J. Geophys. Res.*, *111*, A07204, doi:10.1029/2005JA011196.
- Walén, C. (1944), On the theory of sunspots, *Ark. f. mat. astr. och fysik*, Bd. 30A, No. 15.
- Zettergren, M., and J. Semeter (2012), Ionospheric plasma transport and loss in auroral downward current regions, *J. Geophys. Res.*, *117*, A06306, doi:10.1029/2012JA017637.